Supporting Information

Concerted Proton-Electron Transfer in the Oxidation of Hydrogen-Bonded Phenols

Ian J. Rhile, Todd F. Markle, Hirotaka Nagao, Antonio G. DiPasquale, Oahn P. Lam, Mark A. Lockwood, Katrina Rotter and James M. Mayer*

University of Washington, Department of Chemistry, Box 351700, Seattle, WA 98195, mayer@chem.washington.edu

Supporting Information

I. General Experimental

Unless otherwise noted, reagents were purchased from Aldrich, solvents from Fischer, and deuterated solvents from Cambridge. Tri-*p*-tolylamine was purchased both from Aldrich and Acros. 2-Bromo-4,6-di-*t*-butylphenol was purchased from Lancaster, Inc. *n*-Butyllithium in hexanes was purchased from Acros. Ammonia was purchased from Matheson. Ether was purified by vacuum transfer from sodium benzophenone ketal. $NOPF_6$ was purchased from Alfa Aesar. ^{1}H NMR and ^{13}C NMR spectra were recorded on Bruker AF300, AV300, AV301, DRX499 or AV500 spectrometers at ambient temperatures; chemical shifts are reported relative to TMS in ppm by referencing to the residual solvent signals. Column chromatography used silica gel as the stationary phase.

II. Syntheses.

HOAr-OH,[1] **HOAr-NH$_2$**,[1] **HOAr-im**,[2] and **HOAr-py**[3] are known compounds.

(3,5-Di-*tert*-butyl-2-methoxyphenyl)diphenylmethanol (**MeOAr-OH**). To a solution of 1-bromo-3,5-di-*tert*-butyl-2-methoxybenzene[4] (1.62 g, 5.41 mmol) in 40 mL ether at –78 °C was added 3.39 mL *n*-butyllithium in hexanes (1.6 M, 5.41 mmol). The reaction was allowed to warm to 0 °C for 15 min, and then cooled back to –78 °C. Benzophenone (0.987 g, 5.41 mmol) in 10 mL ether was added and the reaction allowed to come to room temperature. After quenching with aqueous ammonium chloride, the layers were separated, and the aqueous layer was extracted twice with ether. Combined ether layers were washed with saturated aqueous sodium chloride, dried over magnesium sulfate, filtered and concentrated. Column chromatography with 30/1 to 10/1 v/v hexanes/ether afforded the product, 1.77 g (81%). ^{1}H NMR ($CDCl_3$): δ 7.36-7.27 (m, 11 H, Ar–H), 6.60 (s, 1H, O*H*), 6.49 (d, *J* = 2.5 Hz, 1H, Ar–*H*) 3.08 (s, 3H, OCH_3), 1.44 (s, 9H, ^{t}Bu), 1.13 (s, 9H, ^{t}Bu). ^{13}C{^{1}H} NMR ($CDCl_3$): δ 155.4 (MeO*C*), 147.9, 145.0, 142.7, 140.4 (Ph

(1) Rhile, I. J.; Mayer, J. M. *J. Am. Chem. Soc.* **2004,** *126*, 12718-12719.
(2) Benisvy, L.; Bill, E.; Blake, A. J.; Collison, D.; Davies, E. S.; Garner, C. D.; Guindy, C. I.; McInnes, E. J. L.; McArdle, G.; McMaster, J.; Wilson, C.; Wolowska, J. *Dalton Trans.* **2004,** 3647-3653.
(3) Inoue, Y.; Nakano, T.; Tanaka, H.; Kashiwa, N.; Fujita, T. *Chem. Lett.* **2001**, 1060-1061.
(4) Kamaraj, K.; Kim, E.; Galliker, B.; Zakharov, L. N.; Rheingold, A. L.; Zuberbuehler, A. D.; Karlin, K. D. *J. Am. Chem. Soc.* **2003**, *125,* 6028-6029.

C-1; anisole *C*-1, 3, 4, and/or 5), 128.4, 127.8, 127.3 (Ph *C*-2, 3, 4), 124.8 (anisole *C*-6), 88.6 (HO*C*), 63.3 (O*C*H_3), 35.9, 34.5, (*C*Me_3), 32.0, 31.4 (C(*C*H_3)$_3$). Two aromatic ^{13}C NMR peaks are apparently overlapping.

C-(3,5-Di-*tert*-butyl-2-methoxyphenyl)-*C*,*C*-diphenylmethylamine (**MeOAr-NH$_2$**) HCl gas was bubbled through a solution of 0.518 g (1.28 mmol) **MeOAr-OH** in 25 mL Et_2O for 50 minutes. The ether was removed from the green solution on a vacuum line, and fresh ether was vacuum transferred in. Ammonia was bubbled through the solution, and ammonium chloride precipitated out. The mixture was filtered and concentrated. Two columns (1st: 30/1 v/v hexanes/ether, then straight ether; 2nd: 8/1 v/v hexanes/ether) afforded the product, 0.194 g (38%). ^{1}H NMR ($CDCl_3$): δ 7.33-7.26 (m, 11H; Ar–*H*), 6.53 (d, *J* = 2.5 Hz, 1H, Ar–*H*), 2.92 (s, 3H, OC*H*$_3$), 1.43 (s, 9H, ^{t}Bu), 1.13 (s, 9H, ^{t}Bu); N*H*$_2$ protons were not observed. ^{13}C{^{1}H} NMR ($CDCl_3$): δ 156.3 (MeO*C*), 149.1, 143.9, 142.9, 142.3, 127.6, 124.3 (anisole *C*s, Ph *C*-1), 128.5, 127.8, 126.8 (Ph C-2, 3, 4), 68.0, 62.5 (H_2N*C*, O*C*H_3), 35.9, 32.1 (*C*Me_3), 32.1, 31.4 (C(*C*H_3)$_3$).

The iron-bipyridyl and phenanthroline complexes were synthesized according to literature procedures[5] and were used as PF_6^- salts. 10-Methylphenothiazinium tetrafluoroborate was synthesized according to literature procedures.[6]

Triarylamines with varying methoxy groups (N(*p*-$CH_3OC_6H_4$)$_n$(*p*-BrC_6H_4)$_{3-n}$, *n* = 1, 2, 3) were synthesized by CuI-catalyzed addition of $NaOCH_3$ to tri-(*p*-bromophenyl)amine, modified from ref 7. The procedure for tri-*p*-anisylamine is given below. The other *p*-anisylamines were made with fewer equivalents of $NaOCH_3$ and collection of the appropriate spot by column chromatography (24-30/1 v/v hexanes/ether; R_f N(*p*-C_6H_4OMe)$_3$ < N(*p*-C_6H_4OMe)$_2$(*p*-C_6H_4Br) < N(*p*-C_6H_4OMe)(*p*-C_6H_4Br)$_2$ < N(*p*-C_6H_4Br)$_3$).

Tri-*p*-anisylamine. Sodium methoxide was generated by the careful addition of Na (3 g) to dry CH_3OH (13 mL). After an initial burst of heat and H_2 evolution, heating was required to complete reaction. Pyridine (40 mL) was added, followed by copper(I) iodide (2.97 g, 1.5 equiv) and N(*p*-C_6H_4Br)$_3$ (3.00 g, 1 equiv). After refluxing for 2 h, approximately half the solvent was distilled away. Water was added and the product extracted with ether. The ether was washed three times with water and once with saturated aqueous NaCl, and then dried with $MgSO_4$. After concentration, a column (24/1 v/v hexanes/ether) afforded the product, which was recrystallized from hexanes: 1.22 g (34%). ^{1}H NMR (C_6D_6): 7.09 (d, *J* = 9 Hz, 6H), 6.72 (d, *J* = 9 Hz 6H), 3.13 (s, 9H). MS (m/z): 335 (M), 320 (M–CH_3).

Aminium salts were synthesized by $NOPF_6$ oxidation of the corresponding amines.[8] To synthesize tri-*p*-tolylaminium hexafluorophosphate ([N(*p*-$C_6H_4CH_3$)$_3$]PF_6), for example, a suspension of $NOPF_6$ (0.305 g) in CH_2Cl_2 (10 mL) was cooled in a dry ice/acetone bath and purged with N_2. While stirring and continuing purging, a solution of N(*p*-$C_6H_4CH_3$)$_3$ (0.501 g) in methylene chloride (5 mL)

---

(5) DeSimone, R. E.; Drago, R. S. *J. Am. Chem. Soc.* **1970,** *92,* 2343-2352.

(6) Litt, M. H.; Radovic, J. *J. Phys. Chem.* **1974,** *78,* 1750-1754.

(7) (a) Bonhôte, P.; Moser, J.-E.; Humphry-Baker, R.; Vlachopoulos, N.; Zakeeruddin, S. M.; Walder, L.; Grätzel, M. *J. Am. Chem. Soc.* **1999,** *121,* 1324-1336. (b) Bacon, R. G. R.; Rennison, S. C.; *J. Chem. Soc. C* **1969,** 312-315.

(8) (a) Bandlish, B. K.; Shine, H. *J. Org. Chem.* **1977,** *42,* 561. (b) Eberson, L.; Larsson, B. *Acta Chem. Scand., Ser. B* **1986**, *40*, 210. (c) Eberson, L.; Larsson, B. *Acta Chem. Scand., Ser. B* **1987**, *41*, 367.

was added to the suspension slowly. After complete addition, the blue reaction mixture was allowed to warm to room temperature. The reaction was filtered. Ether was added to the filtrate to precipitate $[Ntol_3]PF_6$ as a blue solid, 0.417 g (56%).

III. X-ray Crystal Structures of HOAr-NH_2•$^1/_2$*n*-hexane, HOAr-im•MeOH, and HOAr-py.

General procedure. Crystals were mounted on glass capillaries using Paratone-N® oil and frozen immediately in a cold nitrogen gas stream at 130 K (100 K for **HOAr-py**). Data were collected on an Enraf-Nonius KappaCCD diffractometer (Bruker AXS P8 CCD for **HOAr-py**) with Mo-Kα radiation (λ = 0.71073 Å) utilizing both Φ and Ω scans. Crystal-to-detector distance was 30 mm (60 mm for **HOAr-py**). The data was integrated and scaled using hkl-2000 or hkl-SCALEPACK (SADABS for **HOAr-py**). These programs apply a multiplicative correction factor (S) to the observed intensities (*I*) and has the following form: $S = (e^{-2B(\sin^2\theta)/\lambda^2})/\text{scale}$. S is calculated from the scale and B factor, which is determined for each frame and is then applied to *I* to give the corrected intensity (I_{corr}). Solution by direct methods (SIR97) produced a complete heavy atom phasing model consistent with the proposed structure and refined by full-matrix least-squares based on F^2 (SHELXL-97). All non-hydrogen atoms were refined anisotropically, while all hydrogen atoms except for hydroxyl and amine hydrogen atoms were placed using a riding model. Hydroxyl and amine hydrogen atoms were located from the Fourier difference map and their positions were refined isotropically. Collection and refinement data are given in Table S1. Data for the hydrogen bonds in the molecules are listed in Table S2.

HOAr-NH_2•$^1/_2$ *n*-hexane. X-ray quality crystals were grown from hot hexanes and a colorless crystal 0.42 × 0.28 × 0.28 mm in size was used for data collection. Exposure time was 30 s per degree and the scan width was 2.0˚. Data collection was 91.0% complete to 24.71º in θ. One molecule of *n*-hexane co-crystallized with two molecules of the **HOAr-NH_2**, forming the asymmetric unit.

HOAr-im•MeOH. X-ray quality crystals were grown from hot methanol and a colorless crystal 0.67 × 0.24 × 0.12 mm in size was used for data collection. Exposure time was 30 s per degree and scan width was 2.0˚. Data collection was 89.4% complete to 24.71º in θ. One molecule of methanol co-crystallized with one molecule of **HOAr-im**, forming the asymmetric unit.

HOAr-py. X-ray quality crystals were grown from hot methanol and a pale yellow crystal 0.14 × 0.12 × 0.10 mm in size was used for data collection. Exposure time was 30 s per degree and the scan width was 0.3˚. Data collection was 99.4% complete to 25º in θ. Three independent molecules of the target complex make up the asymmetric unit.

Table S1. Collection and refinement data.

	HOAr-im • CH_3OH	**HOAr-NH_2** • $^1/_2$ hexane	**HOAr-py**
empirical formula	$C_{32}H_{40}N_2O_4$	$C_{60}H_{80}N_2O_2$	$C_{19}H_{25}NO$
formula weight	516.66	861.3	283.4
temperature (K)		130(2)	
wavelength (Å)		0.71073	
crystal description	Prism	prism	prism
color	Colorless	clear, colorless	pale yellow
crystal system	Triclinic	triclinic	monoclinic
space group	P $\bar{1}$	P $\bar{1}$	$P2_1/c$
unit cell dimensions			
a (Å)	9.4740(5)	11.4910(3)	18.492(4)
b (Å)	10.5800(5)	14.9150(7)	10.077(2)
c (Å)	14.7340(11)	15.1270(8)	27.860(6)
α (°)	87.1080(19)	75.3230(16)	90
β□(°)	84.814(2)	79.8130(14)	91.86(3)
γ□(°)	77.8560(18)	74.796(3)	90
volume ($Å^3$)	1437.15(15)	2403.22(18)	5188.8(19)
Z	2	4	12
density (Mg/m^3)	1.194	1.131	1.088
absorption coefficient (mm^{-1})	0.078	0.067	0.066
F(000)	556	890	1848
crystal size (mm)	0.67 × 0.24 × 0.24	0.42 × 0.28 × 0.28	0.14 × 0.12 × 0.10
reflections for indexing	299	1400	383
θ range for data collection (°)	3.09–24.71	2.93–28.28	2.93–25.03
index ranges	$-11 \le h \le 8$	$-13 \le h \le 12$	$-21 \le h \le 22$
	$-11 \le k \le 10$	$-19 \le k \le 14$	$-11 \le k \le 11$
	$-17 \le l \le 16$	$-19 \le l \le 20$	$-33 \le l \le 33$
reflections collected	6608	13928	35348
unique reflections	4381	7470	9080
R_{int}	0.0504	0.0626	0.0615
completeness to θ = 25.00	89.40%	91.10%	99.4
absorption correction		semi-empirical from equivalents	
max/min transmission	0.9815/0.9495	0.9815/0.9724	0.9934/0.9908
refinement method		Full-matrix least-squares on F^2	
data	4381	7470	9080
restraints	0	0	0
parameters	361	565	595
goodness-of-fit on F^2 (*S*)	0.999	1.003	1.026
final *R*	0.0555	0.0585	0.0689
R_w	0.1483	0.1414	0.1724
largest diff. peak and hole (e/A^3)	0.353/–0.281	0.379/–0.324	0.282/–0.186

Table S2. Hydrogen bonding parameters (distances in Å, angles in °).

compound	DH---A[a]	*d*(D-H)	*d*(H---A)	*d*(D---A)	∠(D-H--A)	intermolecular H-bond[b]
HOAr-im• CH_3OH	**O(1)H(1)---N(1)**	0.92(3)	1.80(3)	2.646(2)	153(2)	
	N(2)H(2)---O(4)	0.93(2)	1.93(2)	2.827(3)	161(2)	im**N**H---**O**(H)Me
	O(4)H(4)---O(3_2)[c]	1.01(5)	1.80(4)	2.806(4)	172(2)	MeO**H**---**O**(Me)C_6H_4im
HOAr-py	**O(1)H(1)---N(1)**	1.03(3)	1.58(3)	2.561(3)	156(2)	
	O(2)H(2)---N(2)	0.95(3)	1.68(3)	2.567(3)	154(3)	
	O(3)H(3)---N(3)	0.95(3)	1.70(3)	2.573(3)	151(2)	
HOAr-NH_2• $^1/_2$ hexane	**O(1)H(1)---N(1)**	0.86(2)	1.74(2)	2.550(2)	155(2)	
	O(2)H(2)---N(2)	0.93(2)	1.75(3)	2.613(3)	152(2)	

[a] Donor-acceptor pairs that are bold represent an intramolecular hydrogen bond between a phenol and its pendent base. [b] For intermolecular hydrogen bonds, the donor atom is bold. [c] The MeOH moiety is hydrogen bound to an oxygen atom of an anisyl group in an adjacent asymmetric unit.

IV. Kinetics.

A. **HOAr-NH$_2$** + $[FeL_3]^{3+}$, $[NAr_3]^{\bullet+}$ and $[MPT]^{\bullet+}$ at room temperature.

The Supporting Information of reference 1 presents the method and data for the determination of rate constants for **HOAr-NH$_2$** + $[Fe(bpy)_3](PF_6)_3$, $[Fe(5,5'\text{-}Me_2bpy)_3](PF_6)_3$, $[N(p\text{-}C_6H_4Br)_3]PF_6$, $[N(p\text{-}C_6H_4OMe)(p\text{-}C_6H_4Br)_2]PF_6$, $[N(tol)_3]SbCl_6$, $[N(p\text{-}C_6H_4OMe)_2(p\text{-}C_6H_4Br)]PF_6$, $[N(p\text{-}C_6H_4OMe)_3]PF_6$ at room temperature.

The kinetics for reaction of **HOAr-NH$_2$** + $[Fe(4,7\text{-}Me_2phen)_3](PF_6)_3$ and $[Fe(3,4,7,8\text{-}Me_4phen)_3](PF_6)_3$ were performed under pseudo-first order conditions with 10-50-fold excess of phenol, and fit to first-order kinetics. The observed rate constants at individual concentrations are reported on Tables S3 and S4 and plotted in Figures S1 and S2. The slope of k_{obs} v. [**HOAr-NH$_2$**] is reported as the second-order rate constant.

Table S3. Observed pseudo-first order rate constants for **HOAr-NH$_2$** + $[Fe(4,7\text{-}Me_2phen)_3](PF_6)_3$.

[**HOAr-NH$_2$**][a]	k_{obs} (s^{-1})	σ
0.143	49	1.6
0.286	106	2.5
0.429	160	6.3
0.572	213	8.6
0.715	270	12.3

[a] mM.

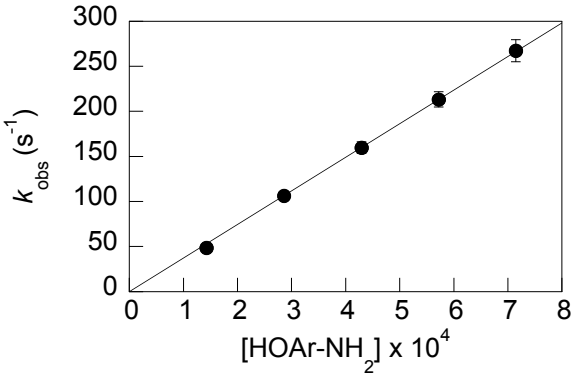

Figure S1. Pseudo first-order rate constants vs. concentration of phenol for **HOAr-NH$_2$** + $[Fe(4,7\text{-}Me_2phen)_3](PF_6)_3$.

Table S4. Second-order rate constants for **HOAr-NH$_2$** + $[Fe(3,4,7,8\text{-}Me_4phen)_3]^{3+}$.

[**HOAr-NH$_2$**][a]	k_{obs} (s^{-1})	σ
0.172	5.01	0.019
0.345	10.07	0.071
0.517	15.46	0.056
0.689	20.26	0.083
0.861	25.4	0.14

[a] mM.

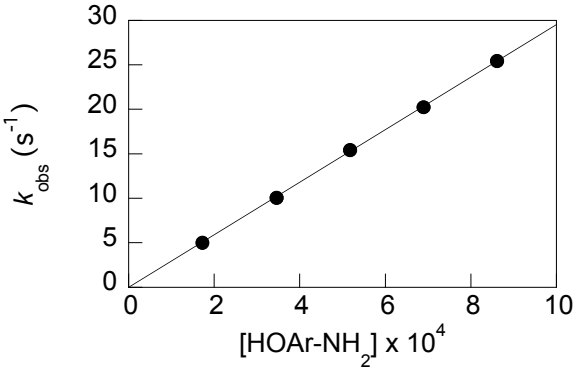

Figure S2. Pseudo first-order rate constants vs. concentration of phenol for **HOAr-NH$_2$** + $[Fe(3,4,7,8\text{-}Me_4phen)_3]^{3+}$.

The kinetics for reaction of **HOAr-NH$_2$** + [MPT]BF$_4$ were performed with 10-50-fold excess of phenol, and fit to opposing second-order kinetics. The rate constants at individual concentrations are reported on Table S5 and plotted in Figure S3.

Table S5. Second-order rate constants for **HOAr-NH$_2$** + [MPT]$^{\bullet+}$.

[**HOAr-NH$_2$**][a]	k (M^{-1} s^{-1})	σ
0.248	3.65×10^4	1.4×10^3
0.496	3.40×10^4	1.1×10^3
0.744	2.90×10^4	1.5×10^3
0.992	2.92×10^4	9.5×10^2
1.24	3.20×10^4	5.3×10^2

[a] mM.

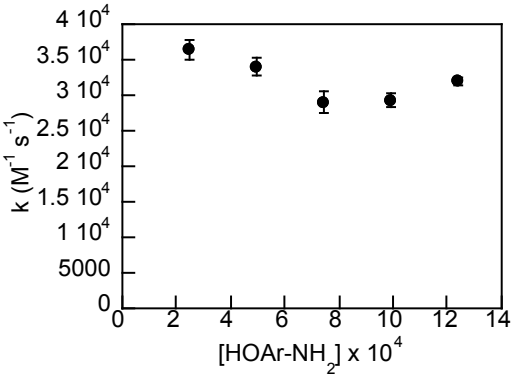

Figure S3. Second-order rate constants vs. concentration of phenol for **HOAr-NH$_2$** + [MPT]$^{\bullet+}$.

The rate kinetics for reaction of **HOAr-im** + [N(*p*-C$_6$H$_4$OMe)$_3$]PF$_6$ were performed with 25-125-fold excesses of phenol, and fit to opposing second-order kinetics. The rate constants at individual concentrations are reported on Table S6 and graphed in Figure S4.

Table S6. Second-order rate constants for **HOAr-im** + [N(*p*-C$_6$H$_4$OMe)$_3$]$^{\bullet+}$.

[**HOAr-im**][a]	k (M^{-1} s^{-1})	σ
0.469	1.03×10^4	3.3×10^2
0.938	1.12×10^4	8.0×10^2
1.41	1.18×10^4	7.5×10^2
1.88	1.10×10^4	4.7×10^2
2.35	1.00×10^4	3.5×10^2

[a] mM

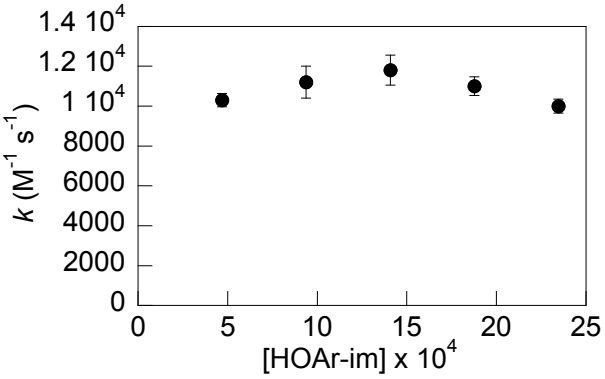

Figure S4. Second-order rate constants vs. concentration of phenol for **HOAr-im** + [N(*p*-C$_6$H$_4$OMe)$_3$]$^{\bullet+}$.

The rate constants for reaction of **HOAr-py** with $[Fe(Me_2bpy)_3](PF_6)_3$, $[Fe(bpy)_3](PF_6)_3$, $[Fe(3,4,7,8\text{-}Me_4phen)_3](PF_6)_3$, and $[Fe(4,7\text{-}Me_2phen)_3](PF_6)_3$ were measured with 2-10-fold excess of phenol, and fit to opposing second-order kinetics. The rate constants for the two reactions at individual concentrations are reported in Table S7 – S10 and plotted in Figures S5–S8.

Table S7. Second-order rate constants for **HOAr-py** + $[Fe(Me_2\text{-}bpy)_3](PF_6)_3$.

[phenol][a]	k (M^{-1} s^{-1})	σ
0.040	6.30×10^5	9.4×10^3
0.081	5.52×10^5	4.8×10^3
0.12	5.7×10^5	1.0×10^4
0.16	5.7×10^5	3.8×10^4
0.20	5.7×10^5	1.8×10^4

[a] (mM)

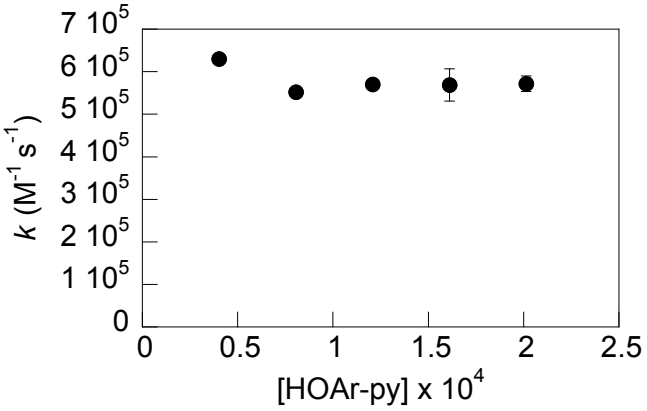

Figure S5. Second-order rate constants vs. concentration of phenol for **HOAr-py** + $[Fe(Me_2\text{-}bpy)_3](PF_6)_3$.

Table S8. Second-order rate constants for **HOAr-py** + $[Fe(bpy)_3](PF_6)_3$.

[phenol][a]	k (M^{-1} s^{-1})	σ
0.021	3.9×10^6	1.9×10^5
0.042	3.8×10^6	2.1×10^5
0.064	4.0×10^6	3.0×10^5
0.085	4.5×10^6	4.1×10^5
0.11	4.9×10^6	4.9×10^5

[a] (mM)

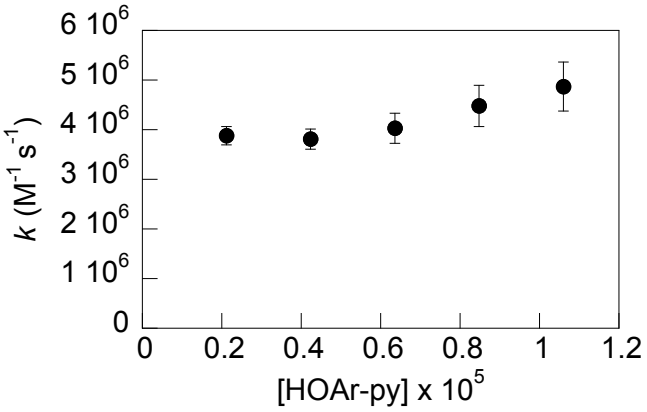

Figure S6. Second-order rate constants vs. concentration of phenol for **HOAr-py** + $[Fe(bpy)_3](PF_6)_3$.

Table S9. Second-order rate constants for **HOAr-py** + $[Fe(3,4,7,8\text{-}Me_4phen)_3](PF_6)_3$.

[phenol][a]	k (M^{-1} s^{-1})	σ
0.388	3.5×10^5	2.9×10^4
0.776	3.1×10^5	1.2×10^4
1.16	3.3×10^5	1.2×10^4
1.55	3.1×10^5	2.6×10^4
1.94	2.8×10^5	6.5×10^4

[a] (mM)

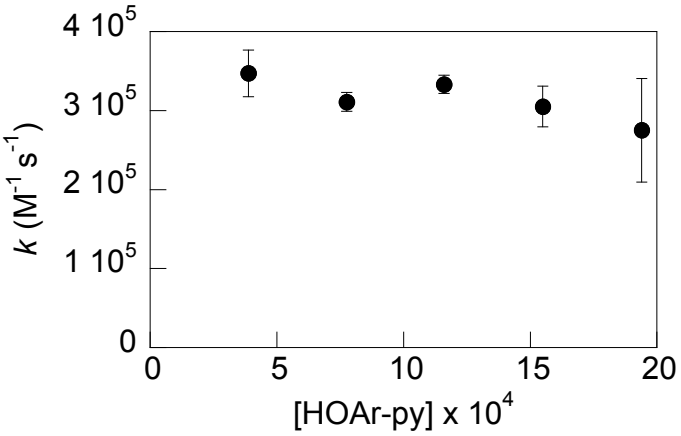

Figure S7. Second-order rate constants vs. concentration of phenol for $[Fe(3,4,7,8\text{-}Me_4phen)_3](PF_6)_3$.

Table S10. Second-order rate constants for **HOAr-py** + $[Fe(4,7\text{-}Me_2phen)_3](PF_6)_3$.

[phenol][a]	k (M^{-1} s^{-1})	σ
0.041	1.9×10^6	3.3×10^5
0.082	2.0×10^6	9.5×10^4
0.123	1.9×10^6	1.4×10^5
0.164	1.7×10^6	1.1×10^5
0.205	1.7×10^6	1.7×10^5

[a] (mM)

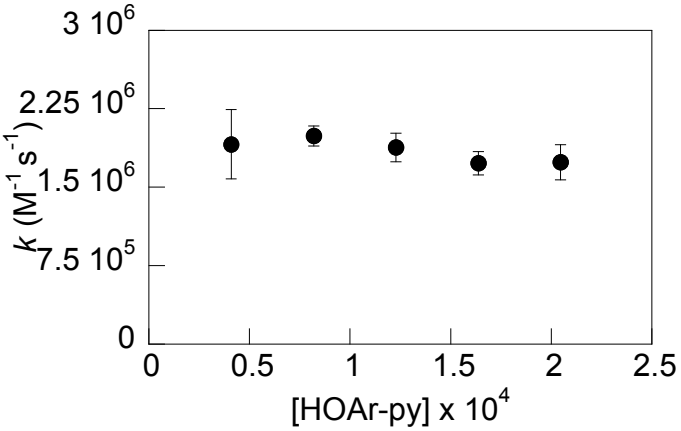

Figure S8. Second-order rate constants vs. concentration of phenol for **HOAr-py** + $[Fe(4,7\text{-}Me_2phen)_3](PF_6)_3$.

B. Temperature dependence experiments

The temperature dependence kinetics for **HOAr-NH_2** were performed under pseudo-first order conditions with a 10-80-fold excess of phenol at various temperatures. Five concentrations were taken at each temperature. The slope of k_{obs} vs. **[HOAr-NH_2]** (y = mx) was taken as the second-order rate constant. The rate constants are listed in Table S11 and plotted in Figure S9. A summary of the rate constants vs. temperature is on Table S12.

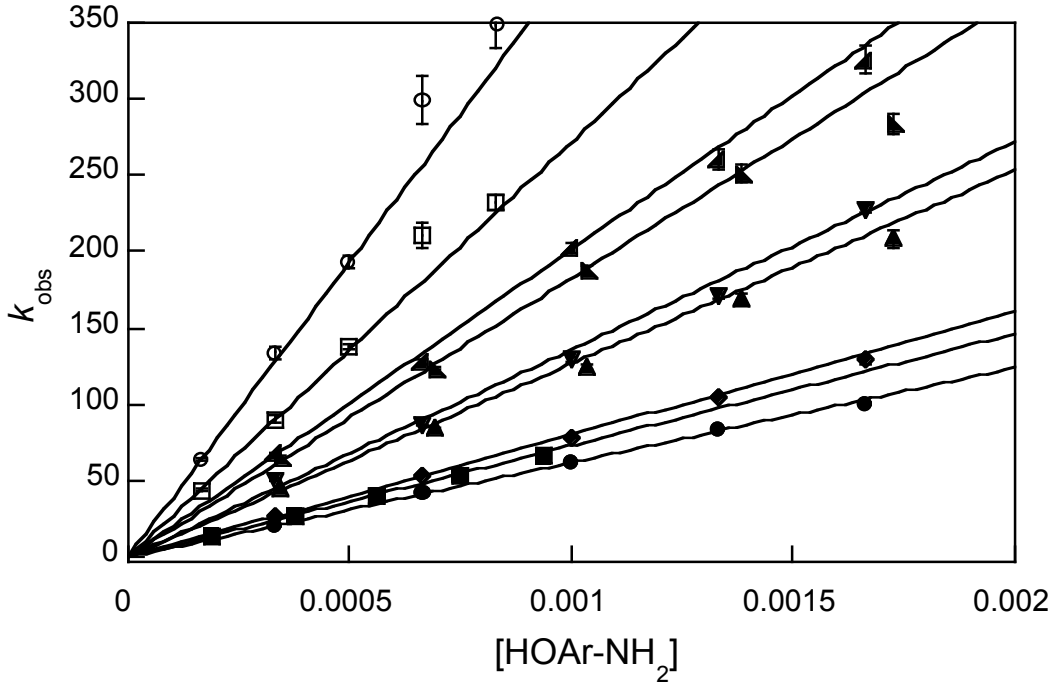

Figure S9. Pseudo-first order rate constants vs. phenol concentration for HOAr-NH_2 + $[N(tol)_3]^{\bullet+}$. Temperatures in K: 279.6 (●), 282.3 (■), 286.5 (◆), 297.1 (▲), 299.2 (▼), 307.4 (◣), 310.2 (◢), 317.7 (○), and 327.0 (□).

Table S11. Pseudo-first order rate constants vs. phenol concentration for **HOAr-NH$_2$** + [N(tol)$_3$]$^{\bullet+}$.

T (°C)	[phenol] (mM)	k_{obs}	σ	T (°C)	[phenol] (mM)	k_{obs}	σ
6.4	0.333	20.7	0.12	34.2	0.346	65.6	0.51
	0.665	42.1	0.55		0.691	123	1.2
	0.998	62.0	0.80		1.04	187	3.4
	1.33	83.8	1.2		1.38	251	6.4
	1.66	100	1.2		1.73	283	6.1
9.1	0.188	14.3	0.19	37.0	0.333	68.1	0.45
	0.375	27.4	0.45		0.665	128	1.8
	0.563	40.7	0.61		0.998	203	3.9
	0.750	53.1	0.78		1.33	261	6.1
	0.938	65.8	3.9		1.66	326	8.4
13.3	0.333	26.9	0.068	44.5	0.166	44.0	0.51
	0.665	53.0	0.27		0.333	90.6	1.8
	0.998	78.1	0.59		0.499	138	2.0
	1.33	105	0.42		0.665	211	8.4
	1.66	129	2.49		0.832	233	4.6
23.9	0.346	44.4	0.14	53.8	0.166	63.5	0.65
	0.691	84.0	0.57		0.333	134	3.6
	1.04	125	1.9		0.499	193	4.2
	1.38	169	3.0		0.665	299	15
	1.73	208	5.3		0.832	347	15
26.0	0.333	50.7	0.26				
	0.665	86.6	0.33				
	0.998	130	1.8				
	1.33	171	2.0				
	1.66	228	2.9				

Table S12. Summary of temperature dependence data for HOAr-NH$_2$ + [N(tol)$_3$]$^{\bullet+}$

T (K)	k (M^{-1} s^{-1})	T (K)	k (M^{-1} s^{-1})
279.6	$(6.2 \pm 0.6) \times 10^4$	307.4	$(1.8 \pm 0.2) \times 10^5$
282.3	$(7.3 \pm 0.7) \times 10^4$	310.2	$(2.0 \pm 0.2) \times 10^5$
286.5	$(8.0 \pm 0.8) \times 10^4$	317.7	$(2.7 \pm 0.3) \times 10^5$
297.1	$(1.3 \pm 0.1) \times 10^5$	327.0	$(3.9 \pm 0.4) \times 10^5$
299.2	$(1.4 \pm 0.1) \times 10^5$		

The temperature dependence of the kinetics for **HOAr-py** + $[Fe(5,5'\text{-}Me_2bpy)_3](PF_6)_3$ were performed with a 2-12-fold excess of phenol at various temperatures. Five concentrations were taken at each temperature, with the exception of the experiments at 14.6 °C where four concentrations were used. The rate constants were fit with opposing second-order kinetics. A set of data at 39.8 °C ([phenol] = 0.12 mM) was excluded because satisfactory fits could not be obtained. The rate constants are presented in Table S13 and plotted in Figure S10. The average of the rate constant were taken as the second-order rate constant and are given in Table S14.

Table S13. Second-order rate constants vs. phenol concentration for **HOAr-py** + $[Fe(Me_2\text{-}bpy)_3]^{3+}$.

T (°C)	[phenol][a]	k (M^{-1} s^{-1})	σ	T ()	[phenol][a]	k (M^{-1} s^{-1})	σ
6.0	0.042	3.56×10^5	3.7×10^3	29.6	0.040	7.9×10^5	7.3×10^3
	0.085	3.46×10^5	6.6×10^3		0.081	6.1×10^5	1.4×10^4
	0.13	3.08×10^5	3.2×10^3		0.12	6.1×10^5	1.7×10^4
	0.17	3.09×10^5	2.8×10^3		0.16	5.8×10^5	1.2×10^4
	0.21	3.62×10^5	8.3×10^3		0.20	5.6×10^5	1.6×10^4
10.0	0.041	3.8×10^5	1.5×10^4	35.0	0.040	6.1×10^5	5.4×10^3
	0.082	3.57×10^5	6.5×10^3		0.081	7.37×10^5	8.6×10^3
	0.12	3.8×10^5	2.3×10^4		0.12	7.9×10^5	2.2×10^4
	0.16	3.7×10^5	1.9×10^4		0.16	7.5×10^5	2.1×10^4
	0.21	3.43×10^5	7.7×10^3		0.20	7.41×10^5	8.8×10^3
14.6	0.042	4.31×10^5	3.8×10^3	39.8	0.030	7.6×10^5	2.0×10^4
	0.085	4.14×10^5	7.2×10^3		0.061	9.0×10^5	5.2×10^4
	0.13	3.95×10^5	8.4×10^3		0.091	1.18×10^6	7.8×10^4
	0.17	3.86×10^5	4.3×10^3		0.15	1.07×10^6	3.7×10^4
24.9	0.041	6.43×10^5	5.8×10^3	45.2	0.030	8.25×10^5	7.5×10^3
	0.082	6.8×10^5	1.1×10^4		0.061	9.4×10^5	3.8×10^4
	0.12	6.7×10^5	1.6×10^4		0.091	1.04×10^6	2.7×10^4
	0.16	6.5×10^5	1.6×10^4		0.12	1.09×10^6	4.9×10^4
	0.20	6.4×10^5	1.2×10^4		0.15	1.27×10^6	5.1×10^4

[a] mM

Table S14. Summary temperature dependence data for **HOAr-py** + $[Fe(5,5'\text{-}Me_2bpy)_3](PF_6)_3$.

T (K)	k (M^{-1} s^{-1})
279.2	$(3.2 \pm 0.5) \times 10^5$
283.2	$(3.7 \pm 0.4) \times 10^5$
287.8	$(4.1 \pm 0.6) \times 10^5$
295.0	$(5.8 \pm 0.9) \times 10^5$
298.1	$(6.6 \pm 1.0) \times 10^5$
302.8	$(6.2 \pm 0.9) \times 10^5$
308.2	$(7.4 \pm 1.1) \times 10^5$
313.0	$(9.7 \pm 1.9) \times 10^5$
318.4	$(1.0 \pm 0.15) \times 10^6$

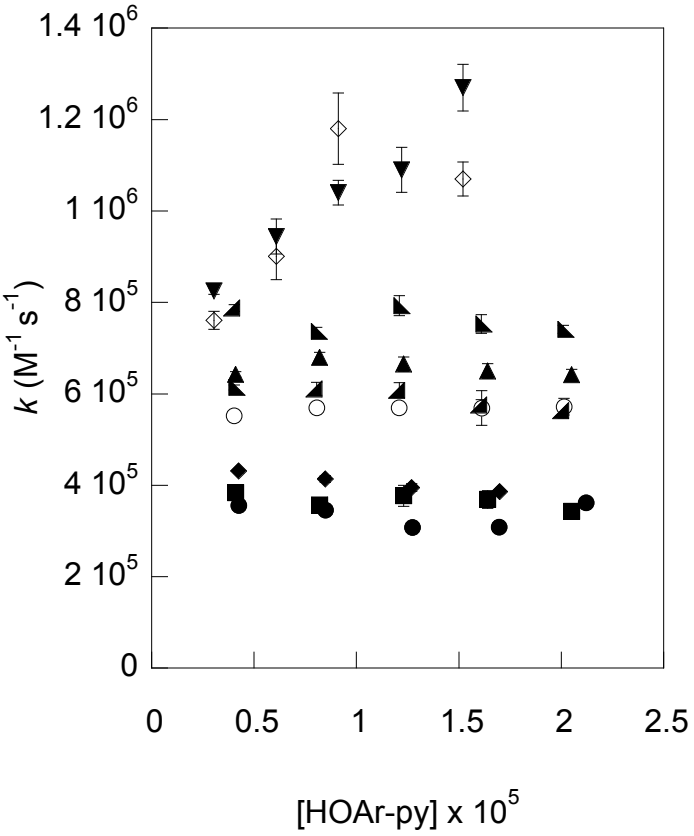

Figure S10. Second-order order rate constants vs. phenol concentration for HOAr-py + $[Fe(Me_2\text{-bpy})_3](PF_6)_3$. Temperatures: 6.0 °C (●), 10.0 °C (■), 14.9 °C (◆), 23 ± 2 °C (○), 24.9 °C (▲), 29.6 °C (◢), 35.0 °C (◣), 39.8 °C (◇), 45.2 °C (▼).

The temperature dependent kinetics for HOAr-im + $[N(p\text{-}MeOC_6H_4)_3]PF_6$ were performed with a 18-110-fold excess of phenol at various temperatures. Five concentrations were taken at each temperature. The rate constants were fit with opposing second-order kinetics. The rate constants are presented in Table S15 and plotted in Figure S11. The average of the rate constant were taken as the second-order rate constant and are presented on Table S16.

Table S15. Second-order order rate constants vs. phenol concentration for **HOAr-im** + $[N(p\text{-}MeOC_6H_4)_3]^{\bullet+}$. (Data for 23 °C is given above).

T (°C)	[phenol][a]	k (M^{-1} s^{-1})	σ
5.0	0.406	3.41×10^3	2.3×10^2
	0.811	3.77×10^3	9.5×10^1
	1.22	3.79×10^3	1.4×10^2
	1.62	4.34×10^3	1.4×10^2
	2.03	4.38×10^3	9.5×10^1
14.6	0.391	5.96×10^3	3.2×10^2
	0.782	6.74×10^3	2.2×10^2
	1.17	7.23×10^3	2.8×10^2
	1.56	7.33×10^3	2.8×10^2
	1.95	7.49×10^3	2.8×10^2
35.2	0.391	1.58×10^4	1.8×10^3
	0.782	1.56×10^4	1.0×10^3
	1.17	1.50×10^4	1.1×10^3
	1.56	1.41×10^4	1.1×10^3
	1.95	1.32×10^4	6.8×10^2

[a] mM

Table S16. Summary of rate constants for temperature dependence.

T (K)	k (M^{-1} s^{-1})
278.2	$(3.9 \pm 0.4) \times 10^3$
287.8	$(6.9 \pm 0.7) \times 10^3$
298.2	$(1.1 \pm 0.1) \times 10^4$
308.4	$(1.5 \pm 0.2) \times 10^4$

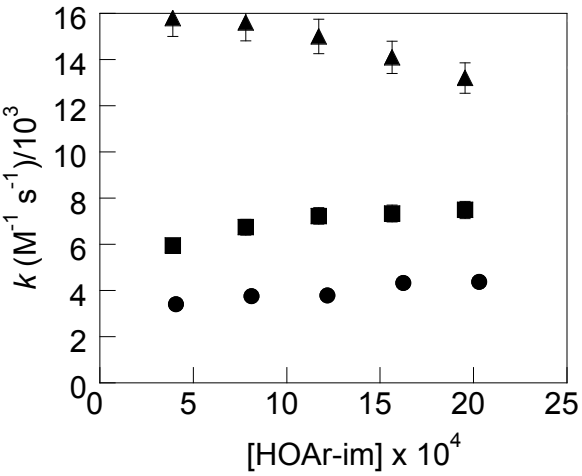

Figure S11. Second-order order rate constants vs. phenol concentration for **HOAr-im** + $[N(p\text{-}CH_3OC_6H_4)_3]^{\bullet+}$. Temperatures: 5.0 °C (●), 14.6 °C (■), 35.2 °C(▲).

C. Isotope effect experiments

In each instance, the kinetics were performed as in the protonated phenols above or as previously reported,[1] but with 0.5-1% v/v aerobic CH_3OD. The control experiments were performed with a 0.5-1% v/v benchtop CH_3OH.

The isotope effect kinetics for **DOAr-ND$_2$ +** [N(*p*-$MeOC_6H_4)_3$]PF_6 (1% CH_3OD) were performed with a 19-97-fold excess of phenol, and fit to opposing second-order kinetics. The rate constants at individual concentrations are reported on Table S17 and plotted in Figure S12.

Table S17. Second-order rate constants vs. concentration of phenol for **DOAr-ND$_2$** + [N(*p*-$C_6H_4OCH_3)_3$]$^{\bullet+}$ in 1% v/v CH_3OD in CH_3CN.

[**DOAr-ND$_2$**]	k ($M^{-1}s^{-1}$)	σ
0.423	6.92×10^2	32
0.845	7.06×10^2	13
1.27	7.06×10^2	3.1
1.69	7.39×10^2	4.6
2.01	7.51×10^2	10

The average value of 7.2×10^2 M^{-1} s^{-1} was corrected for 6.9% CH_3OH in CH_3OD to give 6.9×10^2 M^{-1} s^{-1}.

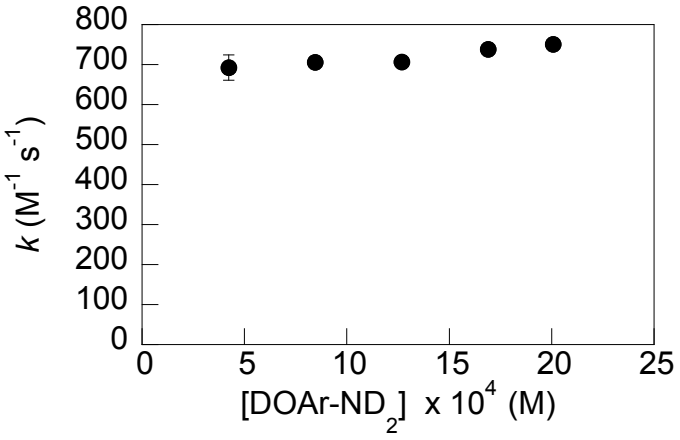

Figure S12. Second-order rate constants vs. concentration of phenol for **DOAr-ND$_2$** + [N(*p*-$C_6H_4OCH_3)_3$]$^{\bullet+}$ in 1% v/v CH_3OD in CH_3CN.

The isotope effect kinetics for **DOAr-ND$_2$ +** [Fe(5,5'-Me_2bpy$)_3$]$(PF_6)_3$ (1% CH_3OD) were performed with a 12-38-fold excess of phenol, and fit to pseudo-first order kinetics. The rate constants at individual concentrations are reported on Table S18 and plotted in Figure S13. The slope is taken as the second-order rate constant.

Table S18. Pseudo first-order rate constants vs. concentration of phenol for **DOAr-ND$_2$** + [Fe(5,5'-Me$_2$bpy)$_3$]$^{3+}$ in 1% v/v CH_3OD in CH_3CN.

[**DOAr-ND$_2$**]	k_{obs} (s^{-1})	σ
0.297	1.83×10^1	0.30
0.396	2.47×10^1	0.40
0.594	3.73×10^1	0.59
0.791	5.13×10^1	0.79
0.940	5.93×10^1	0.94

The slope of 6.5×10^4 M^{-1} s^{-1} was corrected for 6.9% CH_3OH in CH_3OD to give 5.8×10^4 M^{-1} s^{-1}.

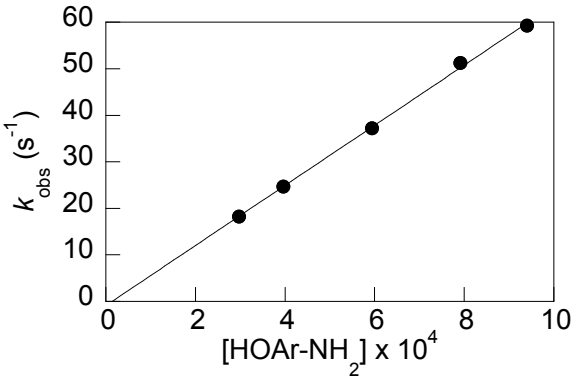

Figure S13. Pseudo first-order rate constants vs. concentration of phenol for **DOAr-ND$_2$** + [Fe(5,5'-Me$_2$bpy)$_3$]$^{3+}$ in 1% v/v CH_3OD in CH_3CN.

The control experiment for **HOAr-NH$_2$ +** [Fe(5,5'-Me$_2$bpy)$_3$](PF$_6$)$_3$ (1% CH_3OH) were performed with a 12-36-fold excess of phenol, and fit to pseudo first-order kinetics. The rate constants at individual concentrations are reported on Table S19 and a graph of the data in Figure S14. The slope is taken as the second-order rate constant.

Table S19. Pseudo first-order rate constants vs. concentration of phenol for **HOAr-NH$_2$** + [Fe(5,5'-Me$_2$bpy)$_3$]$^{3+}$ in v/v 1% CH_3OH in CH_3CN.

[**HOAr-NH$_2$**]	k_{obs} (s^{-1})	σ
0.309	5.11×10^1	0.64
0.412	6.68×10^1	0.25
0.619	9.42×10^1	1.3
0.825	1.19×10^2	1.6
0.979	1.31×10^2	8.5

(0,0) was used as a point for the fit.

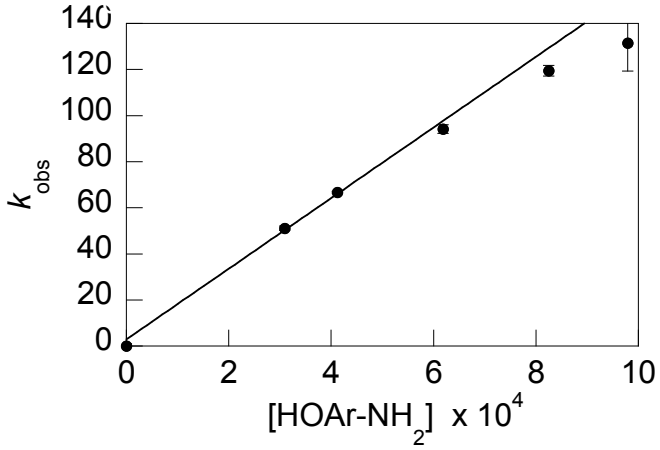

Figure S14. Pseudo first-order rate constants vs. concentration of phenol for **HOAr-NH$_2$** + [Fe(5,5'-Me$_2$bpy)$_3$]$^{3+}$ in 1% v/v CH_3OH in CH_3CN.

The isotope effect experiment for **DOAr-ND$_2$ +** [N(tol)$_3$]PF$_6$ (1% CH_3OD) were performed with a 10-48-fold excess of phenol, and fit to pseudo first-order kinetics. The rate constants at individual concentrations are reported on Table S20 and plotted in Figure S15. The slope is taken as the second-order rate constant.

Table S20. Pseudo first-order rate constants vs. concentration of phenol for **DOAr-ND$_2$** + [Ntol$_3$]$^{\bullet+}$ in 1% v/v CH_3OD in CH_3CN.

[**DOAr-ND$_2$**]	k_{obs} (s^{-1})	σ
0.235	1.31×10^1	0.11
0.469	2.46×10^1	0.11
0.704	3.60×10^1	0.16
0.94	4.54×10^1	0.50
1.11	5.33×10^1	0.90

(0,0) was used as a point for the fit. The slope of 4.7×10^4 M^{-1} s^{-1} was corrected for 6.9% CH_3OH in CH_3OD to give 4.3×10^4 M^{-1} s^{-1}.

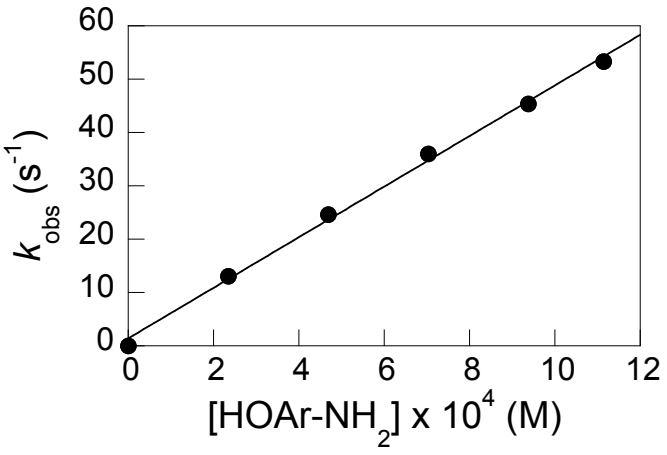

Figure S15. Pseudo first-order rate constants vs. concentration of phenol for **DOAr-ND$_2$** + [N(tol)$_3$]$^{\bullet+}$ in 1% v/v CH_3OD in CH_3CN.

The control experiments for **HOAr-NH$_2$ +** [N(tol)$_3$]PF_6 with 1% protio methanol (CH_3OH) were performed with a 12-55-fold excess of phenol, and fit to pseudo first-order kinetics. The rate constants at individual concentrations are reported on Table S21 and plotted in Figure S16. The slope is taken as the second-order rate constant.

Table S21. Pseudo first-order rate constants vs. concentration of phenol for **HOAr-NH$_2$** + [N(tol)$_3$]$^{\bullet+}$ in v/v 1% CH_3OH in CH_3CN.

[**HOAr-NH$_2$**][a]	k_{obs} (s^{-1})	σ
0.240	33.3	0.25
0.480	59.2	1.3
0.720	86.8	2.0
0.960	107	2.8
1.14	121	3.4

[a] mM

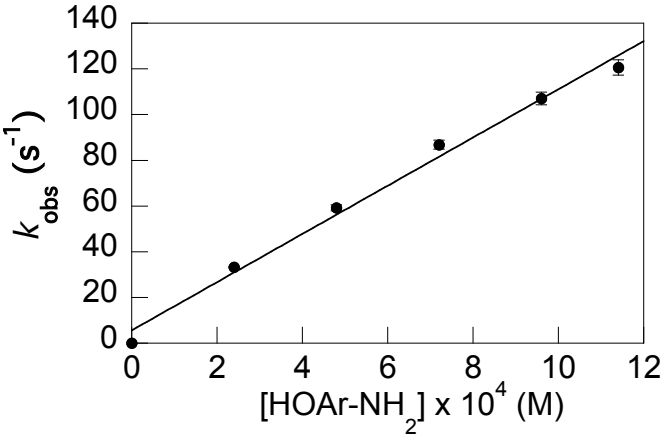

Figure S16. Pseudo first-order rate constants vs. concentration of phenol for **HOAr-NH$_2$** + [N(tol)$_3$]$^{\bullet+}$ in 1% v/v CH_3OH in CH_3CN.

The isotope effect kinetics for **DOAr-py +** $[Fe(5,5'\text{-}Me_2bpy)_3](PF_6)_3$ (0.5% CH_3OD) were performed with a 2-9-fold excess of phenol, and fit to opposing second-order kinetics. The rate constants at individual concentrations are reported on Table S22 and plotted in Figure S17.

Table S22. Second-order rate constants vs. concentration of phenol for **DOAr-py** + $[Fe(Me_2\text{-}bpy)_3](PF_6)_3$ in v/v 0.5% CH_3OD in CH_3CN.

[**HOAr-py**][a]	k ($M^{-1}\,s^{-1}$)	σ
0.0412	2.36×10^5	7.0×10^3
0.0825	2.26×10^5	3.6×10^3
0.124	2.80×10^5	3.1×10^3
0.165	2.42×10^5	4.7×10^3
0.206	2.45×10^5	5.8×10^3

[a] mM

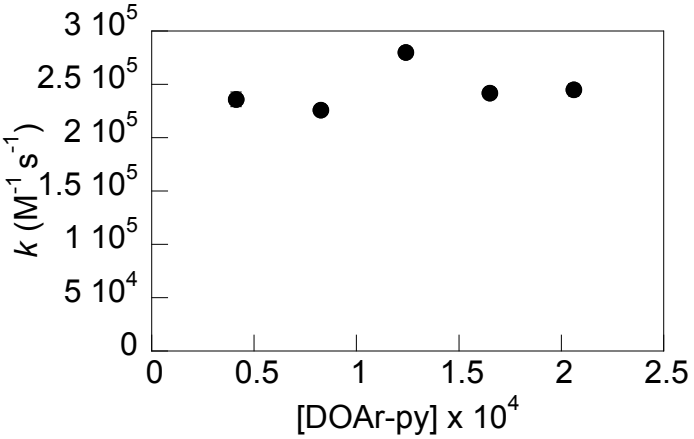

Figure S17. Second-order rate constants vs. concentration of phenol for **DOAr-py** + $[Fe(Me_2bpy)_3]^{3+}$ in 0.5% v/v CH_3OD in CH_3CN.

The isotope effect kinetics for **DOAr-py +** $[Fe(bpy)_3](PF_6)_3$ (0.5% CH_3OD) were performed with a 2-6-fold excess of phenol, and fit to opposing second-order kinetics. The rate constants at individual concentrations are reported on Table S23 and plotted in Figure S18.

Table S23. Second-order rate constants vs. concentration of phenol for **DOAr-py** + $[Fe(bpy)_3](PF_6)$ in v/v 0.5% CH_3OD in CH_3CN.

[**HOAr-py**][a]	k ($M^{-1}\,s^{-1}$)	σ
0.062	1.57×10^6	5.3×10^4
0.12	1.70×10^6	7.1×10^4
0.19	1.6×10^6	1.0×10^5

[a] mM

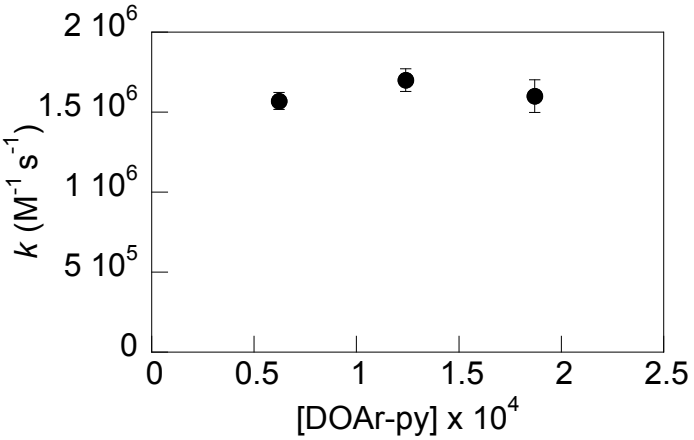

Figure S18. Second-order rate constants vs. concentration of phenol for **DOAr-py** + $[Fe(bpy)_3](PF_6)_3$ in 0.5% v/v CH_3OD in CH_3CN.

The control experiments for **HOAr-py +** $[Fe(Me_2\text{-}bpy)_3](PF_6)_3$, with 0.5% protio CH_3OH, were performed with a 2-11-fold excess of phenol, and fit to opposing second-order kinetics. The rate constants at individual concentrations are reported on Table S24 and plotted in Figure S19.

Table S24. Second-order rate constants vs. concentration of phenol for **HOAr-py** + $[Fe(Me_2\text{-}bpy)_3](PF_6)_3$ in v/v 0.5% CH_3OH in CH_3CN.

[**HOAr-py**][a]	k ($M^{-1}\,s^{-1}$)	σ
0.041	5.00×10^5	2.5×10^3
0.083	5.80×10^5	2.3×10^3
0.12	5.6×10^5	1.9×10^4
0.17	5.8×10^5	1.6×10^4
0.21	6.0×10^5	1.2×10^4

[a] mM

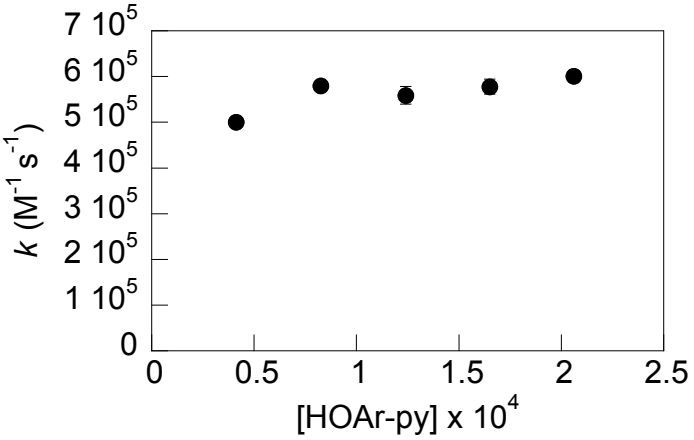

Figure S19. Second-order rate constants vs. concentration of phenol for **HOAr-py** + $[Fe(Me_2\text{-}bpy)_3]^{3+}$ in 0.5% v/v CH_3OH in CH_3CN.

IV. Electrochemistry. Experimental conditions are given in the Experimental section of the paper.

A. Cyclic voltammograms of the phenol derivatives (Figures S20).[a]

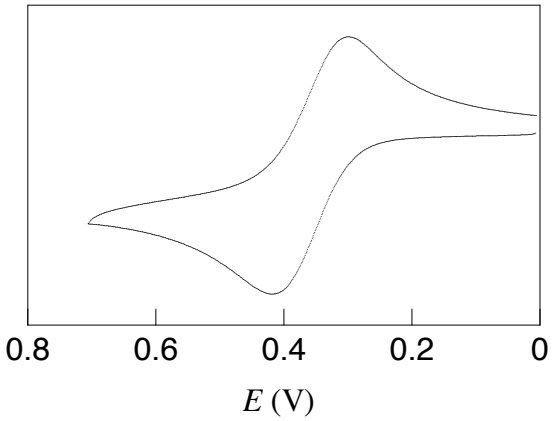

Figure S20a. CV of **HOAr-NH$_2$**.

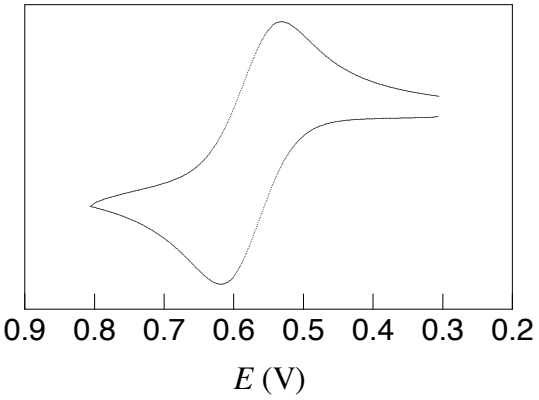

Figure S20b. CV of **HOAr-py**.

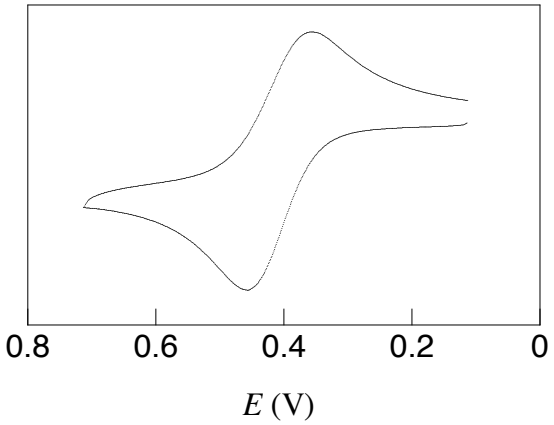

Figure S20c. Cyclic voltammogram of **HOAr-im**.

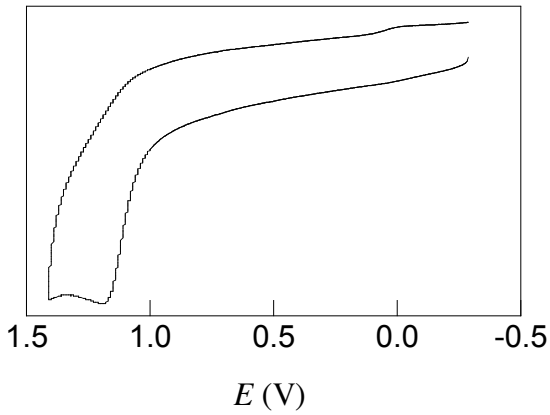

Figure S20d. CV of **MeOAr-NH$_2$**.[b]

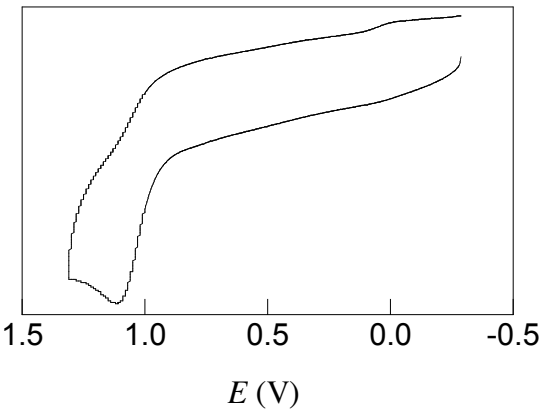

Figure S20e. CV of **HOAr-OH**.[b]

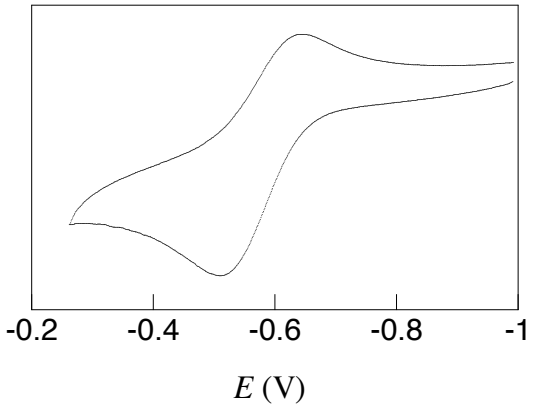

Figure S20f. CV of $^{-}$**OAr-NH$_2$**.[b]

[a] Scan rate = 100 mV s^{-1}. [b] A glassy carbon working electrode (ϕ = 3 mm) was used in these experiments.

B. Potential of $[N(tol)_3]^{\bullet+/0}$ and $[Fe(5,5'\text{-}Me_2bpy)_3]^{3+/2+}$ vs. ionic strength.

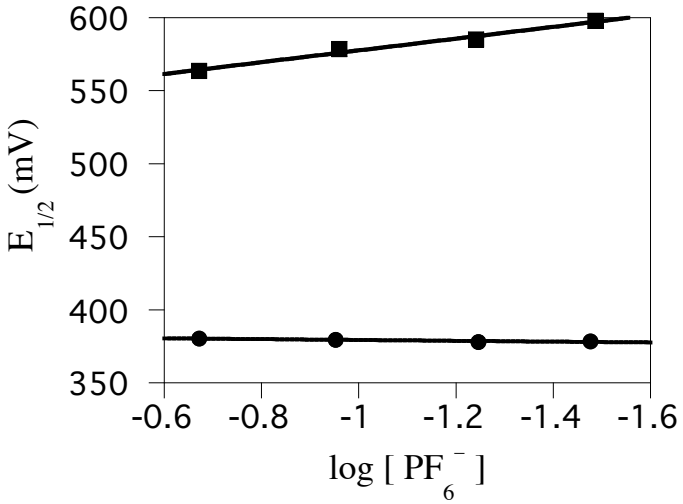

Figure S21. Potential of $[N(tol)_3]^{\bullet+/0}$ (●) and $[Fe(5,5'\text{-}Me_2bpy)_3]^{3+/2+}$(■) vs. log $[PF_6^-]$

C. Variation of driving force with temperature.

See Experimental section of the text for details. The errors on CV derived $E_{1/2}$ are estimated as ± 20 mV, propagation of error yields an uncertainty of 30 mV in driving force. These error bars were confirmed to have a negligible effect on the fitted value of H_{rp} from eq 15 (< 0.5 cm^{-1}) and the effect on λ was within the experimental uncertainty.

Table S25. Driving force (E_{rxn}) as a function of temperature for **HOAr-NH$_2$** + $[N(tol)_3]^{\bullet+}$.

T (°C)	E_{rxn} (mV)
2 ± 1	-10 ± 30
22 ± 1	0 ± 30
49 ± 1	10 ± 30

Table S26. Driving force (E_{rxn}) as a function of temperature for **HOAr-py** + $[Fe(5,5'\text{-}Me_2bpy)_3]^{3+}$.

T (°C)	E_{rxn} (mV)
2 ± 1	-10 ± 30
22 ± 1	-10 ± 30
46 ± 1	0 ± 30

D. Chronoamperometry.

The electrode area of the Pt working electrode and diffusion constants of a oxidative and reductive form of compounds are determined by double potential step chronoamperometry (CA). In CA experiments, potentials $E1$ and then $E2$ are applied and current (i) is measured as a function of time (t). In the diffusion controlled limit at a constant potential, the relationship between i and t is given by the Cottrell equation,[9]

$$i = nFAC\left(\frac{D}{\pi t}\right)^{1/2} \qquad \text{(S1)}$$

where A is the effective area of the working electrode, C is the concentration of the analyte, and D is diffusion constant of the analyte. An i vs $t^{-1/2}$ plot of CA data should yield a simple linear correlation. From such a plot if D is known, A can be determined from the slope of this relation. If A is known D can be determined in a similar fashion.

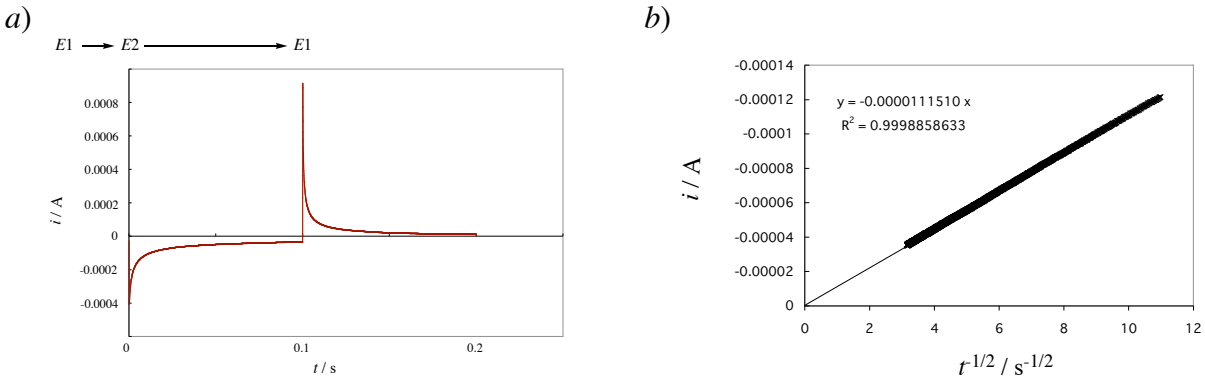

Figure S22. Representative chornoamperometry data: (*a*) i vs t (*b*) plot of i vs $t^{-1/2}$.

(a) Determination of the area of the Pt working electrode.

To determine the area of the working electrode, CA experiments were carried out on ferrocene in 0.6 M tetraethylammonium perchlorate acetonitrile solution. R. Wightman *et al*. have reported the value of D (2.0 x 10^{-5} cm^2 s^{-1}) for 2.0 mM ferrocene under these conditions.[10] CA is measured by using $E1$ = -0.3 and $E2$ = 0.2 V. From these measurements, a mean value of A = 0.02242 cm^2 was found. This is a reasonable value for this electrode (r = 0.8 mm).

(9) Bard, A. J.; Faulkner, L. R. *Electrochemical Methods: Fundamentals and Applications*, 2nd Ed. John Wiley and Sons Inc: New York, 2001.

(10) Wipf, D. O.; Kristensen, E. W.; Deakin, M. R.; Wightman, R. M. *Anal. Chem.* **1988**, *60*, 306-310.

Table S27. Summary CA plots of i vs $t^{-1/2}$ used in determination of the effective area of the Pt disk electrode.

slope	R^2	effective area (cm^2)
0.00001112	0.9994	0.02236
0.00001117	0.9995	0.02246
0.00001116	0.9995	0.02244
0.00001117	0.9995	0.02246
0.00001116	0.9995	0.02244
0.00001109	0.9994	0.02230
0.00001115	0.9995	0.02242
0.00001115	0.9995	0.02242
0.00001116	0.9995	0.02244
0.00001116	0.9995	0.02244

(b) Determination of diffusion constants (*D*).

The diffusion constant for the reduced and oxidized forms of **HOAr-NH$_2$** (D_R and D_O) is obtained from the slope of plots of i vs. $t^{-1/2}$ using the value for A determined above. With C = 2.1 mM we find: $D_R = 1.1 \times 10^{-5}$ cm^2 s^{-1} (Table S28) and $D_O = 8.4 \times 10^{-6}$ cm^2 s^{-1} (Table S29).

Table S28. Summary of i vs $t^{-1/2}$ plots of CA data used to determine D_R of **HOAr-NH$_2$**.

slope	R^2	D_R (cm^2 s^{-1})
8.012E-06	0.9755	1.065E-05
8.000E-06	0.9784	1.061E-05
8.222E-06	0.9831	1.121E-05
7.791E-06	0.9575	1.007E-05

Table S29. Summary of i vs $t^{-1/2}$ plots of CA data used to determine D_O of **HOAr-NH$_2$**.

slope	R^2	D_O (cm^2 s^{-1})
6.880E-06	0.9965	7.850E-06
7.200E-06	0.9969	8.597E-06
7.148E-06	0.9968	8.474E-06
7.393E-06	0.9967	9.065E-06

E. Determination of k_{el}.

Table S30. Electrochemical data derived from cyclic voltammetry (Figure 4a) used to determine k_{el} for **HOAr-NH$_2$** (Figure 4b).

ν (mV s^{-1})	E_{pa} (mV)	E_{pc} (mV)	$E_{1/2}$ (mV)	ΔE_p	I_{pa} (μA)	I_{pc} (μA)	I_{pc} / I_{pa}	R (Ω)	ψ
50	422	318	0.37	104	7.14	6.43	0.901	466	0.484
100	423	307	0.365	116	9.76	8.56	0.877	450	0.368
200	437	295	0.366	143	12.17	10.64	0.8743	454	0.238
500	456	286	0.371	170	14.7	14.26	0.970	436	0.179